JOURNAL OF SYNCHROTRON RADIATION

ISSN 1600-5775

Received 14 November 2014
Accepted 2 March 2015

Keywords: X-ray spectroscopy; energy-dispersive X-ray detector; X-ray emission spectroscopy (XES); resonant inelastic x-ray scattering (RIXS); low-temperature detector; microcalorimeter.

Supporting information: this article has supporting information at journals.iucr.org/s

High-resolution X-ray emission spectroscopy with transition-edge sensors: present performance and future potential

J. Uhlig,[a,b]* W. B. Doriese,[b] J. W. Fowler,[b] D. S. Swetz,[b] C. Jaye,[c] D. A. Fischer,[c] C. D. Reintsema,[b] D. A. Bennett,[b] L. R. Vale,[b] U. Mandal,[a] G. C. O'Neil,[b] L. Miaja-Avila,[b] Y. I. Joe,[b] A. El Nahhas,[a] W. Fullagar,[a,d] F. Parnefjord Gustafsson,[a] V. Sundström,[a] D. Kurunthu,[a] G. C. Hilton,[b] D. R. Schmidt[b] and J. N. Ullom[b]

[a]Department of Chemical Physics, Lund University, Lund, Sweden, [b]National Institute of Standards and Technology, 325 Broadway, MS 817.03, Boulder, CO 80305, USA, [c]Material Measurement Laboratory, National Institute of Standards and Technology, Gaithersburg, MD 20899, USA, and [d]RSPSE, Australian National University, Canberra, ACT 0200, Australia. *Correspondence e-mail: jens.uhlig@chemphys.lu.se

X-ray emission spectroscopy (XES) is a powerful element-selective tool to analyze the oxidation states of atoms in complex compounds, determine their electronic configuration, and identify unknown compounds in challenging environments. Until now the low efficiency of wavelength-dispersive X-ray spectrometer technology has limited the use of XES, especially in combination with weaker laboratory X-ray sources. More efficient energy-dispersive detectors have either insufficient energy resolution because of the statistical limits described by Fano or too low counting rates to be of practical use. This paper updates an approach to high-resolution X-ray emission spectroscopy that uses a microcalorimeter detector array of superconducting transition-edge sensors (TESs). TES arrays are discussed and compared with conventional methods, and shown under which circumstances they are superior. It is also shown that a TES array can be integrated into a table-top time-resolved X-ray source and a soft X-ray synchrotron beamline to perform emission spectroscopy with good chemical sensitivity over a very wide range of energies.

1. Introduction

X-ray emission spectroscopy (XES) analyzes the X-ray spectrum generated when outer-shell electrons fill an empty core state (de Groot & Kotani, 2008; Sa, 2014). A wide variety of particles or X-ray sources can be used to generate the essential core hole. It can be generated by, for example, broad-band generators like X-ray tubes (Als-Nielsen & McMorrow, 2011), the electrons of a scanning electron microscope (Wollman *et al.*, 2000; Newbury *et al.*, 2005) [in this context known as wavelength-dispersive or energy-dispersive X-ray spectroscopy (WDX/EDX)] or laser-based pulsed X-ray sources (Uhlig *et al.*, 2013; Sa, 2014). The following discussion will focus on, but not be limited to, the photon-in/photon-out approach using X-ray radiation as excitation. XES can be used to investigate bulk materials under a broad range of environmental conditions. The spectrum of the emitted X-rays reveals valuable information about the energy and density of the occupied orbitals from which these electrons originate and is therefore sensitive to chemical information including among other things coordination, oxidation and spin state (de Groot & Kotani, 2008; Sa, 2014; Bergmann & Glatzel, 2009; Als-Nielsen & McMorrow, 2011; Vankó *et al.*, 2006, 2013; Gallo & Glatzel, 2014).

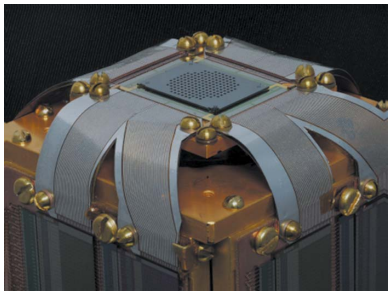

© 2015 International Union of Crystallography

electronic reprint

The improved technology and theoretical understanding of XES has led to an increased demand for experimental installations with sufficient energy resolution to analyze the spectrum of the emitted secondary radiation. At experimental stations with a selectable monochromatic excitation, the addition of XES allows for the use of more techniques like, for example, high-energy-resolution fluorescence detection (HERFD) spectroscopy or resonant inelastic X-ray scattering (RIXS) (Bergmann & Glatzel, 2009; Glatzel *et al.*, 2012). Historically, high-resolution XES has been limited to high-flux X-ray sources including beamlines at large-scale facilities, *e.g.* synchrotrons and free-electron lasers, or demanded excitation from highly radioactive materials, focused sources or a combination thereof (Sa, 2014; Vankó *et al.*, 2013; Kleymenov *et al.*, 2011; Glatzel *et al.*, 2012). These limitations have mostly been caused by the low efficiency of detection systems with sufficient spectral resolution, and extreme and expensive measures are being undertaken to overcome these limitations (ESRF, 2014; Alonso-Mori *et al.*, 2012*a*). While the most detailed information can be extracted when the instrumental resolution is narrower than the lifetime broadening of the line in question, in many cases slightly poorer energy resolution is sufficient. In practice it may be desirable to trade some energy resolution for dramatically increased detection efficiency and therefore reduced requirements on the beam flux. A high excitation flux used on a very small sample spot puts a high demand on the radiation hardness of the materials to be studied, or requires large sample volumes and rapid sample replacement.

This paper discusses and compares contemporary energy-dispersive (ED) low-temperature-detector (LTD) technology designed for high count rates with wavelength-dispersive (WD) technology to indicate the advantages and drawbacks of these two detection approaches. In particular, the potential efficiency advantages of emerging LTD array technologies are highlighted and it is shown that the resolution limits and early results from these devices compare favorably with many elemental line widths.

WD spectrometers use optical elements and position-sensitive or spatially scanned detectors to achieve energy resolution. The relevant technologies for soft X-rays and hard X-rays differ significantly. Soft X-rays of a few 100 eV (XUV) up to $\sim$1.5 keV are dispersed by use of gratings in large vacuum chambers. These are based on grazing-angle reflections and thus require long pathlengths. Surface imperfections do not allow the same approach for hard X-ray radiation, which instead utilizes Bragg diffraction. High efficiency requires a curved scatterer so that the Bragg condition can be met for one energy at a range of positions on the optical component. The size of crystalline optics is limited by, for example, the bending radius of single-crystal materials, the quality of the bent-crystalline media and the spatial and financial resources available. Several large research facilities have developed specialized beamlines with Johann or von Hamos type spectrometers that combine multiple crystals (Alonso-Mori *et al.*, 2012*b*; ESRF, 2014; Bergmann & Cramer, 1998). Crystal *d*-spacing and elemental absorption edges further complicate the design of a WD analyzer in the energy region close to 2 keV. The resolution of WD analyzers depends on the geometry of the setup, typically allowing a maximum spot size of the exciting beam at the sample position of several tens of micrometers in the dispersive direction (Kleymenov *et al.*, 2011). By contrast, an ED spectrometer is able to observe a highly diffuse (many millimeters) beam spot on a sample with no loss in performance, which has profound consequences both for synchrotron-based XES of radiation-sensitive samples and for XES performed with unfocused laboratory-scale X-ray sources.

In many scenarios the X-ray flux available to excite a sample is limited by source characteristics, *e.g.* small laboratory sources, bending-magnet beamlines, sources with special temporal characteristics, or very high energy beamlines. Radiation-sensitive samples including biological materials can also effectively limit the permissible X-ray flux. High detection efficiency is needed for the outgoing secondary X-rays in these scenarios. The detection efficiency of ED devices can be much higher than those of WD approaches because ED detectors do not suffer placement constraints or the Bragg–Darwin losses (Darwin, 1914) typical for narrow-band spectral designs.

Most energy-dispersive detectors rely on charge generation in a semiconductor such as silicon or germanium. Stochastic processes during the creation of the charge cloud from an initial interaction (usually photoelectric or Compton) limit the energy resolution possible with this approach to levels inadequate for many X-ray spectroscopies including XES and X-ray absorption spectroscopy (XAS) (Ahmed, 2014; Janesick, 2001; Fraser *et al.*, 1994; Fullagar *et al.*, 2008). The best achievable resolution for detectors based on silicon is $\sim$125 eV at 6 keV (Fano, 1947; van Roosbroeck, 1965; Lechner *et al.*, 1996).

The operating principle and resolution limits of emerging energy-dispersive low-temperature sensors are fundamentally different and more favorable. In microcalorimeter LTDs the energy of an absorbed photon is distributed among low-energy modes in the absorber (thermalized), and the thermal energy is measured by resistive or magnetic transduction. The resulting thermal flow to a cold bath or a dynamic electrical bias cools the pixel by a nearly exponential temperature decay to its quiescent state [for a schematic see Fig. 1(*a*)]. In a transition edge sensor the temperature rise of the thin sensing bilayer stays within the very steep transition from superconducting to normal conducting state allowing for the necessary precision measurement (Bennett *et al.*, 2012). Fig. 1(*b*) shows the typical electrical response of a single detector during an absorption event. To achieve useful system count rates and collection areas, arrays of pixels are required. Instruments based on arrays as shown in Fig. 1(*c*) have emerged very recently.

In the following, the spectral resolution, collection efficiency and count-rates of LTDs are compared with those of WD techniques. For many applications this technology is not only a viable alternative but also can enable new science. This paper focuses on transition edge sensor microcalorimeters because this low-temperature-sensor technology provides at

electronic reprint

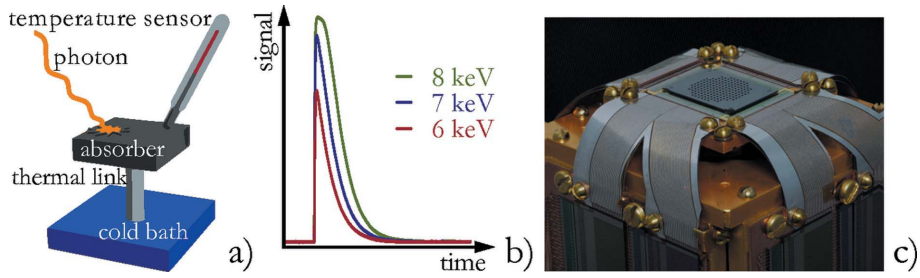

Figure 1
(*a*) Diagram of a single microcalorimeter pixel. The photon is thermalized in a high-Z absorber, typically bismuth or gold. The absorbing film is thermally connected to a thin-film thermometer and these two elements comprise a pixel. Each pixel is connected to the cold bath by an engineered thermal link. The carefully measured integral under the signal shown in (*b*) varies with the energy and allows retrieval of the photon energy. (*c*) Photograph of a microcalorimeter array package (Uhlig, 2011).

the moment the most favorable combination of maturity and performance for XES. However, other types of microcalorimeters, particularly those based on magnetic transduction (Bandler *et al.*, 2012), are an active topic of research and may offer better performance in the future.

2. Energy resolution

The energy resolution of a properly designed microcalorimeter is limited by power fluctuations between the sensor and thermal bath and by broad-band noise contributions from Johnson fluctuations or the read-out amplifier. The energy resolution is proportional to $(k_B T^2 C)^{1/2}$ where C is the device heat capacity and T is the temperature (Moseley *et al.*, 1984). The constant of proportionality depends on the details of the temperature transduction. The thermometer in a transition edge sensor (TES) is a thin metal film electrically biased between the superconducting and normal states.

Because of the finite temperature width of the resistive transition in a TES, it can be shown that sensor resolution is proportional to $(E_{max})^{1/2}$ where E_{max} is the largest energy the device can absorb before losing sensitivity at the top of the resistive transition (Ullom *et al.*, 2005). In the simplest picture of TES operation the resolution of a particular device designed for E_{max} is constant for photon energies below E_{max}. In practice, the saturation point is not so rigidly defined. The resolution begins to degrade due to nonlinearity before reaching E_{max} and some sensitivity is preserved at even higher energies. Recent developments in pulse-processing algorithms show the potential for achieving good energy resolution in pulses traditionally considered saturated (Bandler *et al.*, 2006).

A TES detector designed for 5900 eV recently achieved a resolving power of $E/\Delta E \simeq 3700$, or 1.6 eV full width at half-maximum (FWHM) (Smith *et al.*, 2012). This observed Mn $K\alpha$ energy resolution is shown in Fig. 2 as a red star. The predicted energy resolution as a function of energy is shown as a solid red line based on $E^{1/2}$ scaling of this result (Ullom *et al.*, 2005). Approximately the same resolution is expected for this device at 600 eV. If the same device had been designed with a saturation energy of 600 eV instead, the expected resolution would be better than 0.51 eV.

A different device optimized for a lower E_{max} showed 0.9 eV FWHM at 1.5 keV (Bandler *et al.*, 2013) and is also

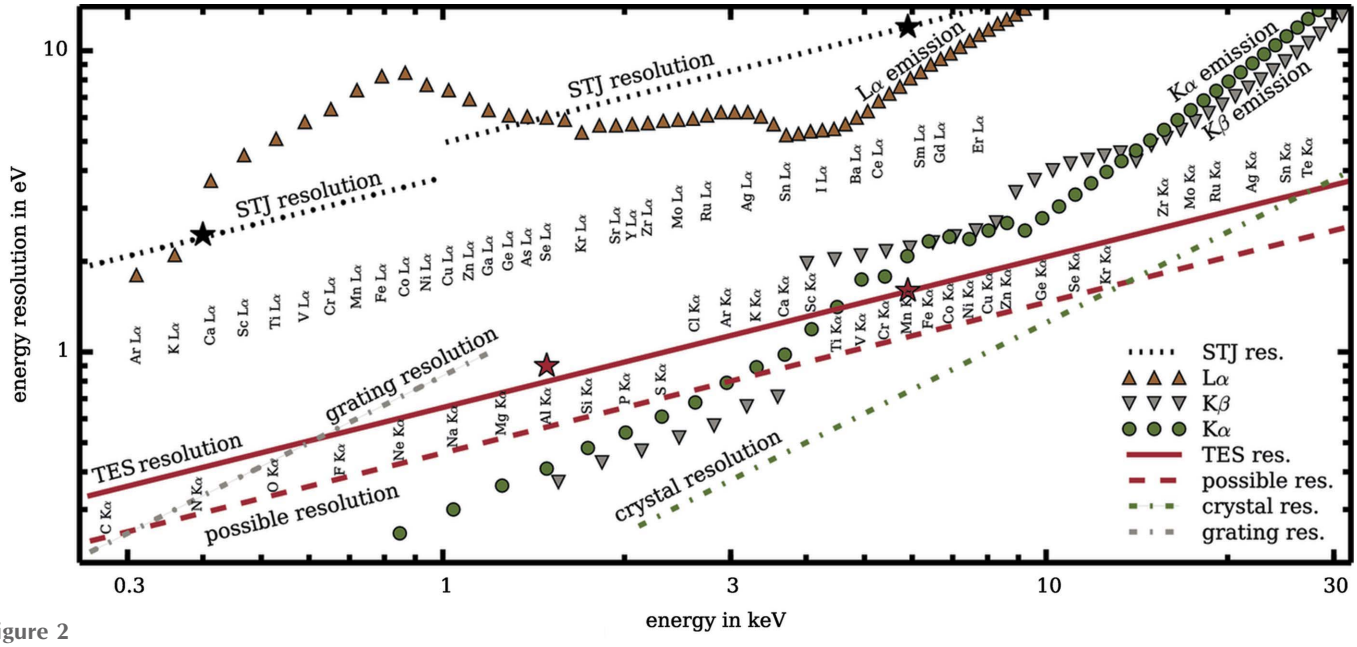

Figure 2
Present and future resolution of microcalorimeter detectors compared with natural line widths of $K\alpha$-, $K\beta$- and $L\alpha$-lines of a number of elements. Resolving powers of 8000 (green dash-dot) and 1200 (grey dash-dot) are shown which are realistic for a high-efficiency crystal analyzer and grating, respectively.

electronic reprint

shown as a red star in Fig. 2. Both results lie close to the solid red line, confirming the validity of the scaling argument. While these single-pixel results are the best TES-based resolution values achieved to date, we caution that these performance levels are not yet routine, particularly in multi-pixel instruments. An average resolution of 2.6 eV at 5.9 keV was obtained in a multi-pixel demonstration (Stiehl *et al.*, 2012). However, the potential of TES instruments is accurately captured by the red line in Fig. 2. Also shown in Fig. 2 is a dashed red line corresponding to speculative future resolution values for TES microcalorimeters, that anticipates a resolution reduction by 0.7 if the transition temperature of the result of Smith *et al.* (2012) is reduced from 100 to 50 mK. Operating temperatures below 50 mK are more challenging than 100 mK but still readily achievable using modern cryogenics.

The intrinsic lifetime broadenings of the $L\alpha$, $K\beta$ and $K\alpha$ transition lines from the xraylib database (Schoonjans *et al.*, 2011) are shown as triangles and circles in Fig. 2 for comparison. TES microcalorimeters already achieve an energy resolution significantly better than all the $L\alpha$ linewidths, and their resolution falls below the $K\alpha$ linewidths for elements above Ti. The dashed red curve indicates that the potential TES resolution is narrower than the intrinsic $K\alpha$ linewidths for elements above Ar. The performance of TES microcalorimeters is thus already good enough to resolve most of the intrinsic linewidths shown in Fig. 2 and that ambitious but realistic improvements in TES performance will leave only first- and second-row $K\alpha$ linewidths unresolved.

The green dot-dashed line in Fig. 2 corresponds to $E/\Delta E = 8000$. This is a reasonable resolving power for a high-efficiency crystal-based spectrometer and is sufficient to resolve all the natural linewidths. This value was taken as typical for a spectrometer with several overlapping non-perfect crystalline analyzers in Johann geometry or a multi-element von Hamos design (Kleymenov *et al.*, 2011). As with all Bragg analyzers, throughput and energy resolution can be interchanged to optimize for a particular experiment or technique.

Fig. 2 does not show the resolution possible with more conventional direct detectors like silicon drift detectors (SDDs) because the resolution of these devices is too poor to fit in the displayed range (Newbury *et al.*, 2005). A modern high-quality SDD has 125 eV FWHM resolution at 5.9 keV which cannot resolve XES features (Oxford, 2014; Ketek, 2014; Amptek, 2014).

Another type of low-temperature detector, the superconducting tunnel junction (STJ), has been used previously for beamline science (Lordi *et al.*, 2003; Shiki *et al.*, 2012). Like a SDD, the resolution of an individual STJ is limited by Fano statistics in the creation of excitations, and scales as the square root of the energy of the absorbed photon. The purpose of this paper is not a comprehensive comparison of detector technologies but we briefly comment on the energy resolution of STJs. At 400 eV, resolution as good as 2.45 eV FWHM has been demonstrated although values of 5–10 eV are more common (Verhoeve *et al.*, 2010; Carpenter *et al.*, 2013; Shiki *et al.*, 2012). Achieving good resolution at energies above 1 keV has proven difficult for STJs due to a variety of factors. The best STJ resolution achieved to date at 5.9 keV is 12 eV FWHM in an unusual device geometry that has not been explored further (Angloher *et al.*, 2002). A more typical STJ resolution at 5.9 keV is 16.6 eV FWHM (Verhoeve *et al.*, 2010). The black stars in Fig. 2 show the resolution results of Verhoeve *et al.* (2010). The dotted black line shows the expected $E^{1/2}$ scaling with a discontinuity near 1 keV to reflect performance differences at high and low energies. It can be seen that STJs do not resolve most of the natural linewidths in the plot including all the linewidths above about 1 keV. While not suitable for XES, the resolution and high per pixel count rates of STJs are well suited to some other applications such as partial fluorescence yield absorption spectroscopy.

3. Collecting efficiency

The very high X-ray-collecting efficiency of a TES-array spectrometer is its principal advantage over a wavelength-dispersive spectrometer based on a grating or crystals. Here, in comparing efficiency among technologies, we use the following definition of total collecting efficiency: the fraction of the total 4π sr (Ω) solid angle around the sample that is intercepted by the spectrometer at each energy times the quantum efficiency (QE) of the spectrometer's various elements. Included in the QE are the absorption efficiency of detectors, reflectivity of mirrors, gratings and crystals, and the transmission, T, of media such as windows and air. In addition, if a spectrometer must be scanned in energy, the total efficiency is divided by the number of energy steps of typical width required to produce the spectrum. For this we estimate the step width to be the Darwin width of the crystal or the typical slit settings. For our estimations we use a typical collection width for a single emission line (*e.g.* 30 eV at 6 keV), the mode in which many experiments are performed today.

The wide energy acceptance of energy-dispersive TES detectors poses new opportunities and also challenges. The ability to measure several different spectral lines simultaneously will open new scientific possibilities, contribute to measurement efficiency, and enable intensity comparisons between widely separated energy features. However, in many scenarios, unwanted photons will be present along with the photons of interest, and TES spectrometers must have sufficient count-rate capability to measure both the wanted and unwanted populations or else their effective collecting efficiency will be smaller than their physical efficiency. Count rates are further discussed in the next section.

For soft X-rays of a few hundred eV up to $\sim$2 keV ruled gratings presently dominate XES instrumentation. This important range includes the $K\alpha$ lines of C, N and O and $L\alpha$ lines of the $3d$ transition metals. An example of a high-collection-efficiency grating spectrometer is the variable-line-spacing (VLS) spectrometer designed for beamline 8 at the Advanced Light Source (Fuchs *et al.*, 2009). Table 1 compares its efficiency with that of a contemporary NIST TES array. At the N $K\alpha$ line (400 eV) the VLS spectrometer collects a solid angle of 11.2 mrad $\times$ 18.0 mrad with a total QE of 0.052 (including the reflectivity of the focusing mirror and grating

electronic reprint

Table 1
Comparison of the total collecting efficiencies of the TES soft-X-ray (sub-keV) spectrometer array installed at APS 29-ID and a representative high-efficiency grating spectrometer [the VLS grating of ALS BL8.0 (Fuchs *et al.*, 2009)].

The TES array has 240 sensors, each of which has an active area of 104 μm × 84 μm and unity QE for sub-keV X-rays. The solid-angle coverage (Ω) of the TES array assumes a sample distance of 2 cm, the minimum practical distance for most samples

	C $K\alpha$	N $K\alpha$	O $K\alpha$
E (eV)	275	400	525
TES $\Omega/4\pi$ sr	4.2×10^{-4}	4.2×10^{-4}	4.2×10^{-4}
T 300 nm Al	0.072	0.35	0.58
TES total efficiency	3.0×10^{-5}	1.5×10^{-4}	2.4×10^{-4}
VLS $\Omega/4\pi$ sr	1.6×10^{-5}	1.6×10^{-5}	1.6×10^{-5}
VLS total efficiency	9.9×10^{-7}	8.3×10^{-7}	7.5×10^{-7}

Table 2
Comparison of the total collecting efficiencies at 5.9 keV of the TES hard-X-ray spectrometer array presently used in the NIST laser laboratory and two representative high-efficiency crystal spectrometers [the five-crystal Johann-geometry spectrometer at ESRF ID26 (Kleymenov *et al.*, 2011) and the 16-crystal von Hamos spectrometer at the LCLS (Alonso-Mori *et al.*, 2012*a*,*b*)].

Details of the estimates can be found in the text and the supporting information. The solid-angle coverage (Ω) of the TES array assumes a sample distance of 2 cm, the minimum practical distance for most samples.

	Johann 5 crystals	von Hamos 16 crystals	TES array
E (keV)	5.9	5.9	5.9
$\Omega/4\pi$ sr per collection step	3.1×10^{-3}	2.2×10^{-4}	4.7×10^{-3}
QE	∼0.1	∼0.1	0.80
Collection steps	60	–	–
Total efficiency	5.2×10^{-6}	2.2×10^{-5}	3.8×10^{-3}

and the QE of the CCD detector). The grating does not need to be scanned in energy to collect an XES spectrum. Thus the total collecting efficiency of this VLS spectrometer is 8.3×10^{-7} of all photons emitted into the N $K\alpha$ line. This spectrometer achieves a resolving power of ∼1000 across the sub-keV band, or ΔE FWHM = 0.4 eV at 400 eV. The NIST 240-TES soft-X-ray spectrometer recently deployed to beamline 29-ID at the Advanced Photon Source (APS) has a total collecting efficiency of 1.5×10^{-4}, or more than two orders of magnitude higher. Each TES has a collimated active area of 104 μm × 84 μm and a 1 μm-thick Bi absorber that provides unity absorption for sub-keV X-rays. The cryogenic TESs are protected from infrared photons by three 100 nm freestanding Al filters. Although the samples are held in a UHV chamber, the present incarnation of the APS spectrometer includes a Moxtek AP3 (one-atmosphere) vacuum window for the safety of the spectrometer during beamline commissioning; this will be removed for future UHV operation and thus its absorption is not included in the efficiency calculations in Table 1. The minimum distance between sample and the TES array is 2 cm. This TES array is designed for energy resolution of about 1.0 eV across the sub-keV X-ray band with $E_{\max} \simeq 2$ keV.

For X-ray energies above 2.5 keV a variety of bent-crystal Bragg-diffraction geometries are used. The three most common are the Johann, Johannson and von Hamos geometries. Detailed descriptions of each can be found in the literature (Hayashi *et al.*, 2004; Hudson *et al.*, 2007; Schülke, 2007; Huotari *et al.*, 2005; Alonso-Mori *et al.*, 2012*b*). Unless extreme designs are chosen [*e.g.* the 72-crystal spectrometer at ESRF ID-20 (ESRF, 2014)], the overall efficiencies of these spectrometers typically fall within the same order of magnitude.

Table 2 compares the efficiency of a 240-TES hard-X-ray spectrometer installed in a time-resolved XAS experiment at NIST (Miaja Avila *et al.*, 2013, 2015) with two representative high-efficiency crystal spectrometers [the five-crystal Johann-geometry spectrometer at ESRF ID26 (Kleymenov *et al.*, 2011) and a von Hamos spectrometer installed at the XPP beamline at the Stanford Linear Accelerator Center (SLAC) (Alonso-Mori *et al.*, 2012*a*,*b*)]. The crystal spectrometers achieve total collecting efficiencies (for one emission line of 30 eV width) of $\sim 5.2 \times 10^{-6}$ and $\sim 2.2 \times 10^{-5}$, respectively (see the supporting information). By contrast, the TES array has a total efficiency of 3.8×10^{-3}, more than two orders of magnitude higher. Each TES has a collimated active area of 320 μm × 305 μm and a 4 μm-thick Bi absorber. As in the soft-X-ray TES array, three 100 nm-Al filters are required to block infrared loading. Here, a 150 μm Be vacuum window allows the spectrometer to observe samples at ambient pressure. This TES array is designed for energy resolution of ∼3 eV FWHM at 5.9 keV.

An energy range in which TES spectrometers have additional advantages is ∼1.5–2.5 keV, which covers the K-line emission of Si, P and S and is difficult to access *via* gratings or crystals. Energies above 1.5 keV become increasingly difficult for gratings due to decreasing X-ray reflectivity and surface imperfections in the gratings. The common crystal materials that are obtainable in very high quality at practical prices *via* the semiconductor industry are Si and Ge. Both have a minimum energy for Bragg reflection (⟨111⟩ plane, normal incidence) of 2.0 keV and 1.9 keV, which is close to their respective absorption edges. Physical restraints due to the high diffraction angle often set the practical limit closer to 2.3–2.5 keV.

Fig. 3 shows the efficiency of microcalorimeter instruments at different energies. The plot contains the hard X-ray array with and without a Moxtek AP3.3 vacuum window (marked as 3 eV system) as well as the soft X-ray system and a comparison with the diffractive analyzers. Future LTD X-ray spectrometers will be even larger and more capable.

4. Count rates

Without the spectral windowing of dispersive optical elements, count rate capability is an important metric for TES performance. The maximum count rate for a TES spectrometer depends on a variety of factors. Count rate and energy resolution for each pixel and of the array as a whole are discussed.

A rule of thumb for the maximum count rate per pixel without significant dead-time or resolution degradation is $1/20\tau$ where τ is the 1/e recovery time of a pulse [see Doriese *et*

electronic reprint

al. (2009) and supporting information]. The recovery time depends on measurable parameters such as the device heat capacity and bias power. In a single TES with $\tau = 200 \times 10^{-6}$ s, spectral resolution as good as 2.3 eV at 6 keV has been achieved at 100 Hz and 99.6% photon acceptance rate (Lee *et al.*, 2014). A complete theory exists to predict τ in the small signal limit (Irwin & Hilton, 2005). For a TES microcalorimeter pixel the required dead-time depends on the details of the pulse recording/processing algorithms. While a detailed discussion is beyond the scope of this paper, a brief note on this topic can be found in the supporting information. Models for other detector types are debated in the literature (see, for example, Sobott *et al.*, 2013; Neri *et al.*, 2010; Kishimoto, 1997; Bateman, 2000).

An attractive quality of TESs is the availability of SQUID-multiplexer readout. In time-, frequency- and code-division SQUID multiplexing, multiple sensors are measured with a single amplifier chain. Multiplexing has enabled large TES arrays (Bennett *et al.*, 2012; Holland *et al.*, 2013) because it reduces the number of readout amplifiers and the number of connections to the cryogenic detector package. Because amplifier bandwidth is always finite, multiplexed readout imposes particularly strict lower limits on τ. The specifications of the ongoing *ATHENA* project (den Herder *et al.*, 2012) provide a useful guide to likely TES performance on the few-year timescale. Anticipated performance levels include recovery times τ near 200×10^{-6} s, multiplexing factors of 30–40 sensors per amplifier chain, and total array sizes of a thousand or more TESs. The total count rate of such a spectrometer will exceed 10^5 Hz for a source obeying Poisson temporal statistics. In addition to time-, frequency- and code-division multiplexing at MHz frequencies, other multiplexing techniques are under development based on microwave readout techniques with potentially orders of magnitude larger bandwidth (Noroozian *et al.*, 2013). While less mature, these techniques may enable significantly faster sensors and larger arrays.

Cross-talk is present in practical multiplexed arrays and pulse pileup has to be considered at high count rates. Higher count rates are possible if some resolution degradation from cross-talk among pixels and pileup within a pixel can be tolerated. Traditional signal processing for TESs and most LTDs relies on an optimal filter constructed from knowledge of the average pulse shape and noise (Szymkowiak *et al.*, 1993). This type of filtering requires the digitization of complete pulse records that are free from pileup pulses. In addition, the optimal filter is often constructed in such a way that longer time records give better resolution (Doriese *et al.*, 2009). As a result, traditional pulse processing for TESs is extremely sensitive to pileup and the output count rate suffers at high input rates.

Pulse pileup is significantly easier to address in sensors with a linear response to the deposited energy. Pulse-processing algorithms have recently been developed that can be applied to TES pulses in the presence of the decaying tail of a preceding pulse (Tan *et al.*, 2008; Alpert *et al.*, 2013). However, TESs are sometimes nonlinear; for example, when measuring photons with energy near E_{max} where resolving power is highest. Pulse-processing algorithms for nonlinear detectors in the presence of pileup is an active research area. Similarly, work is also ongoing on algorithms for the recovery of high spectral resolution without the strict trade-off between record length and resolution (Alpert *et al.*, 2013).

The maximum count rate observed in wavelength-dispersive systems depends on many design parameters and especially the sample under study. Specialized high-flux beamlines like ID26 at the ESRF (Kleymenov *et al.*, 2011) can reach MHz count rates if studying highly concentrated and radiation resilient samples. More typical count rates are around a few kHz. Energy-dispersive silicon drift detectors are typically operated with peaking times of a few microseconds to preserve their 125 eV energy resolution (Amptek, 2014), resulting in count rates of at most a few 100 kHz. Very new systems reduce the shaping time and with it the energy resolution to achieve a throughput of >1 MHz (Krings *et al.*, 2014; Bertuccio *et al.*, 2015). As discussed above, the next generation of TES array detectors will offer similar count rates, but with energy resolution appropriate for XES.

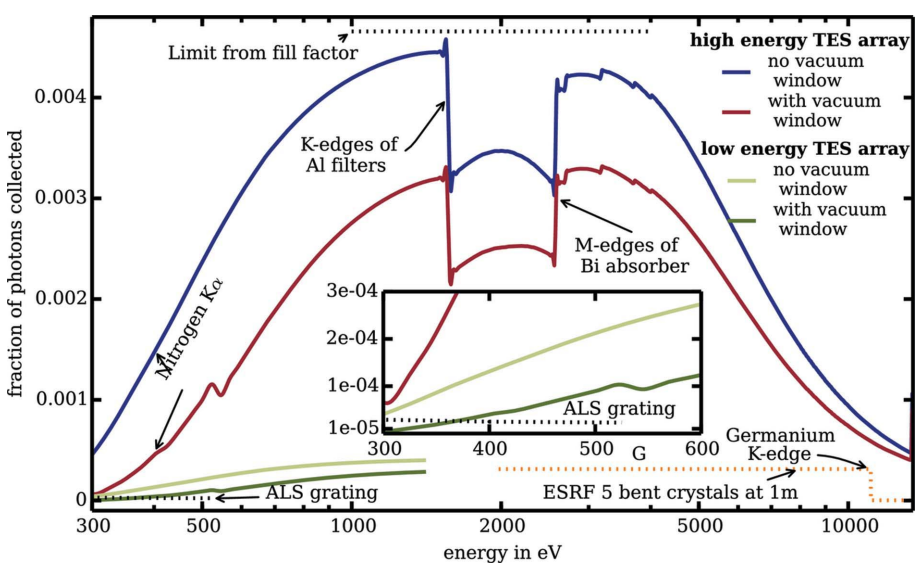

Figure 3
Comparison of the detection efficiency for two contemporary microcalorimetric systems each in freestanding (with vacuum window) and windowless operation. The efficiency limit only determined by the detector fill factor is indicated (with unity absorption and without filter). Two wavelength-dispersive systems designed for high efficiency are shown (see text).

5. Measurements

Here, we show two datasets that demonstrate TES-based XES below

electronic reprint

10 keV and below 1 keV. The first demonstration used a broad-band laboratory excitation source; the second used narrow-band excitation at a synchrotron bending-magnet beamline.

5.1. Hard X-ray emission spectroscopy with a plasma source with sub-picosecond timing structure

For analyzing the time evolution of photo-driven chemical reactions, it is often desirable to use X-ray techniques to obtain element-specific information about atomic structure and electronic activity (Chen *et al.*, 2001; Canton *et al.*, 2013, 2015; Vankó *et al.*, 2013). Laser-driven ultrashort-pulse laboratory X-ray sources are promising tools for studying photo-activity because they are naturally synchronized to an exciting optical laser pulse. To this end we developed a robust X-ray source based on 800 nm, 50 fs Ti:sapphire laser pulses focused on a water jet target. The source produces X-ray pulses of sub-picosecond duration; details have been published by Fullagar *et al.* (2007, 2008) and Uhlig *et al.* (2011). By pairing the source with a TES microcalorimeter spectrometer, both time-resolved absorption spectroscopy (Uhlig *et al.*, 2013) and emission spectroscopy are possible in a laboratory setting.

To demonstrate XES at the Fe $K\beta$ line, we selected a target of ferric oxide (Fe_2O_3), an iron III complex, in a polymer matrix. The target was excited by broad-band bremsstrahlung X-rays generated by the water-jet X-ray source. The microcalorimeter spectrometer was oriented toward the sample and at 90° to the excitation beam so that direct X-rays from the source were not observed. The distance between the spectrometer and sample was 8 cm.

The measured X-ray emission spectrum is shown in Fig. 4. The challenge and strength of direct detection devices is the collection of all emitted photons. The left-hand inset shows all the collected photons in 1 eV bins; the Fe $K\alpha$ peak dominates the full spectrum as expected. The $K\beta$ spectrum is detailed enough to permit chemical analysis and shows a prominent $K\beta'$ feature, the signature of a high-spin iron complex (Haldrup *et al.*, 2012; Vankó *et al.*, 2006, 2013). The right-hand inset shows the 7.1 keV region of the spectrum with a smoothed line to guide the eye. This reveals features likely to be $K\beta_{2,5}$ or even $K\beta''$ lines; these lines are three orders of magnitude weaker than the $K\alpha$ feature. The energy resolution in this early measurement was only 6 eV. The spectrometer is presently capable of resolution better than 4 eV and still better performance is possible as indicated in Fig. 2. The spectrum in Fig. 4 was acquired over 8 h, at 5 Hz pixel^{-1} limited by the source. However, subsequent increases in the array size ($\times$12) and the intensity of the exciting beam (flux rate $\times$100) will allow similar spectra to be captured in less than 1 min.

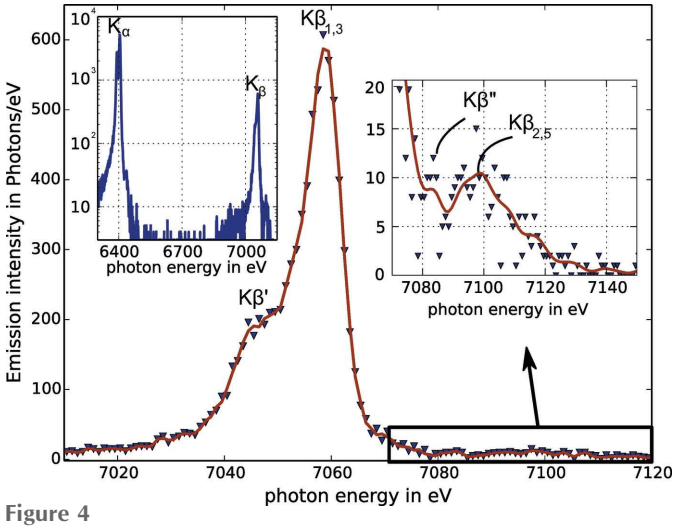

Figure 4
X-ray emission spectrum of Fe_2O_3. The material is identified as a high-spin complex from the prominent $K\beta'$ feature. The left-hand inset shows the full $K\alpha/\beta$ range of the same spectrum. The right-hand inset shows an expanded region of the same spectrum. After re-binning, the weaker $K\beta_{2,5}$ and $K\beta''$ features are evident.

5.2. Nitrogen emission spectroscopy

A TES microcalorimeter spectrometer was installed in 2011 and is currently operated at the bending-magnet beamline U7A of the National Synchrotron Light Source (Fischer, 2014). The microcalorimeter instrument has added XES capability to U7A, where the soft X-ray energy range includes the emission from ubiquitous carbon, nitrogen and oxygen. Non-resonant nitrogen emission can be used to fingerprint many compounds in scientific, industrial and security applications.

To demonstrate the ability of TESs to perform XES below 1 keV, we chose two nitrogen-bearing compounds used in explosives: ammonium nitrate (NH_4NO_3) and RDX ($C_3H_6N_6O_6$). While the security relevance of these compounds is obvious, they also provide well defined and different chemical environments for the constituent nitrogen. In particular, ammonium nitrate contains nitrogen atoms in both highly oxidized and highly reduced environments.

The compounds were deposited on a cleaned Si[001] wafer, dried and introduced into the vacuum of the beamline. The spectrometer contained 45 TES pixels 5 cm from the sample with 320 × 305 µm active area each and was oriented at 90° to the excitation beam with the sample normal oriented at 45° to the excitation beam. The material between the sample and detectors consisted of 300 nm of aluminium and a Moxtek AP3.3 vacuum window. Hence, the experimental configuration was generally representative of future installations of microcalorimeter instruments and enabled a robust XES capability at a beamline that was previously considered too dim for this experimental technique. The primary excitation was 2×10^{10} photons s^{-1} in a few millimeters spot at 425 eV, but harmonics of the primary energy were also present and these excited transitions above 425 eV. The acquisition periods for the NH_4NO_3 and RDX spectra were 29 min and 23 min, respectively. At the time of the measurements, the spectrometer at U7A contained 45 active pixels; the currently installed array contains 240 pixels. The energy-dispersive operating principle of TESs allows the simultaneous collection of X-rays over the full energy range of the spectrometer. As a result, X-rays from carbon, nitrogen and oxygen were

electronic reprint

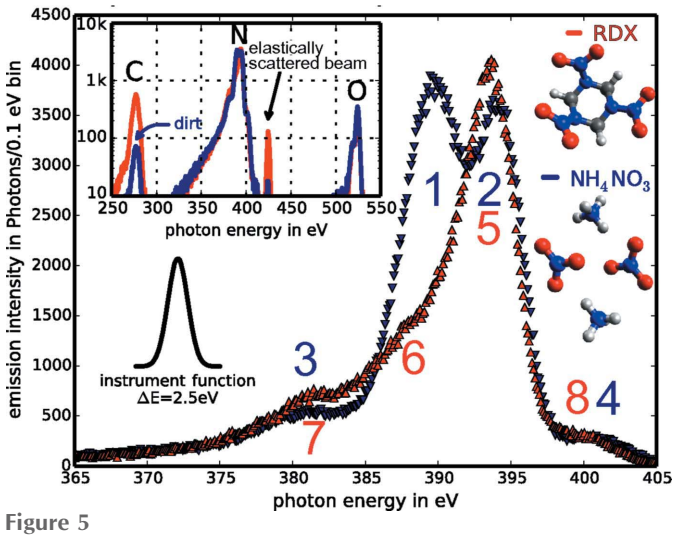

Figure 5
Nitrogen emission spectra of ammonium nitrate (blue) and RDX (red) obtained with the TES array. Fine structure due to local chemical environment is clearly visible and distinct between the two compounds (see text for identification of the numbered features). The different chemical structures are recognizable in the molecular cartoons on the right. The 2.5 eV instrumental response function is shown on the left. The inset shows the same emission spectra with an expanded energy range; the reflected beam and the main emission lines are marked. The spectra of ammonium nitrate and RDX were collected in 29 and 23 min, respectively, with 2×10^{10} photons s^{-1} input from a bending-magnet beamline using a 45 pixel TES detectors with pixel size 320 × 305 µm.

collected as shown in the inset to Fig. 5. The relative intensities of the different elemental lines can be used to identify the approximate ratio between the different atoms of the compound if adjusted for emission probability and window transmission.

Vila *et al.* performed an XES study of these compounds using a grating spectrometer (Vila *et al.*, 2011) at an undulator beamline. With ∼1000× higher excitation flux than used in our 45 pixel demo they achieved similar signal-to-noise ratios in slightly longer (30 min) acquisition time. Their study included a comparison with theoretical calculations and proposed an identification of the components of the spectrum. In our spectrum of (NH_4NO_3) two strong features (1 and 2) can be identified. Referring to the calculations from Vila *et al.* (2011), the features 2, 3 and 4 are associated with the highly oxidized N in the nitrate moiety while feature 1 is associated with the highly reduced N in the ammonia group. Because RDX lacks the variety of nitrogen environments found in ammonium nitrate, the RDX spectrum contains only one dominant peak, feature 5, although smaller features, 6–8, are clearly distinguishable. All spectral features identified in our data are in excellent agreement with the measurements of Vila *et al.* (2011).

From Fig. 5 we conclude that TESs can not only distinguish nitrogen-containing compounds but also can collect high-quality spectra for scientific interpretation and comparison with theoretical models. However, even better spectral performance is possible. The detector used in the experiment was designed for a saturation energy near 10 keV and the 2.5 eV instrument response function (also shown in Fig. 5) reflects this large dynamic range. As discussed previously, TES detectors optimized for a lower saturation energy of 600 eV could achieve resolution as good as 0.6 eV. With the high collection efficiency of large arrays, it is possible to collect very weak or attenuated signals. Signal attenuation might arise from operating the detector outside of a UHV chamber. An example of the latter case is the identification and study of materials in a helium-filled environment. The absorption of nitrogen $K\alpha$ X-rays in 3 cm of helium at 1 atm is 50%. Pathlengths and attenuation factors of this magnitude are quite acceptable for a microcalorimeter spectrometer. In contrast, likely pathlengths in a wavelength-dispersive instrument are much longer, so the increased attenuation poses a greater experimental challenge.

6. Conclusions

Contemporary microcalorimeter arrays offer a viable alternative to wavelength-dispersive X-ray energy analyzers for XES. In photon-starved experiments or in work with radiation-sensitive samples they can be the detector of choice, thanks to extremely high efficiency combined with adequate energy resolution, easy handling and simple physical alignment. Microcalorimeter arrays have begun to find XES applications, when paired with laboratory and ultrafast sources, electron microscopes and synchrotron beamlines. The broad energy acceptance changes not only how X-ray emission spectra are acquired but also makes microcalorimeters uniquely suited as general purpose X-ray spectrometers.

Acknowledgements

We acknowledge support from the NIST Innovations in Measurement Science program and an ERC Advanced Investigator Grant No. 226136 to VS. JU gratefully acknowledges the continued funding from the Knut and Alice Wallenberg Foundation.

References

Ahmed, S. N. (2014). *Physics and Engineering of Radiation Detection*, 2nd ed. New York: Academic Press.
Alonso-Mori, R. *et al.* (2012*a*). *Proc. Natl Acad. Sci. USA*, **109**, 19103–19107.
Alonso-Mori, R., Kern, J., Sokaras, D., Weng, T.-C., Nordlund, D., Tran, R., Montanez, P., Delor, J., Yachandra, V. K., Yano, J. & Bergmann, U. (2012*b*). *Rev. Sci. Instrum.* **83**, 073114.
Alpert, B. K., Horansky, R. D., Bennett, D. A., Doriese, W. B., Fowler, J. W., Hoover, A. S., Rabin, M. W. & Ullom, J. N. (2013). *Rev. Sci. Instrum.* **84**, 056107.
Als-Nielsen, J. & McMorrow, D. (2011). *Elements of Modern X-ray Physics*, 2nd ed. Hoboken: John Wiley and Sons.
Amptek, (2014). *Amptek XR-100SDD*, http://www.amptek.com/products/xr-100sdd-silicon-drift-detector/, accessed: 08/10/14.
Angloher, G., Huber, M., Jochum, J., Rudig, A., von Feilitzsch, F. & Mossbauer, R. L. (2002). *AIP Conf. Proc.* **605**, 23–26.
Bandler, S., Adams, J., Bailey, C., Busch, S., Chervenak, J., Eckart, M., Ewin, A., Finkbeiner, F., Kelley, R., Kelly, D. P., Kilbourne, C., Porst, J. P., Porter, F., Sadleir, J., Smith, S. & Wassell, E. (2013). *IEEE Trans. Appl. Supercond.* **23**, 2100705.

electronic reprint

Bandler, S. R., Figueroa-Feliciano, E., Iyomoto, N., Kelley, R. L., Kilbourne, C. A., Murphy, K. D., Porter, F. S., Saab, T. & Sadleir, J. (2006). *Nucl. Instrum. Methods Phys. Res. A*, **559**, 817–819.

Bandler, S., Irwin, K., Kelly, D., Nagler, P., Porst, J.-P., Rotzinger, H., Sadleir, J., Seidel, G., Smith, S. & Stevenson, T. (2012). *J. Low Temp. Phys.* **167**, 254–268.

Bateman, J. E. (2000). *J. Synchrotron Rad.* **7**, 307–312.

Bennett, D. A. *et al.* (2012). *Rev. Sci. Instrum.* **83**, 093113.

Bergmann, U. & Cramer, S. P. (1998). *Proc. SPIE*, **3448**, 198–209.

Bergmann, U. & Glatzel, P. (2009). *Photosynth. Res.* **102**, 255.

Bertuccio, G., Ahangarianabhari, M., Graziani, C., Macera, D., Shi, Y., Rachevski, A., Rashevskaya, I., Vacchi, A., Zampa, G., Zampa, N., Bellutti, P., Giacomini, G., Picciotto, A. & Piemonte, C. (2015). *J. Instrum.* **10**, P01002.

Canton, S. E. *et al.* (2013). *J. Phys. Chem. Lett.* **4**, 1972–1976.

Canton, S. E. *et al.* (2015). *Nat. Commun.* **6**, 6359.

Carpenter, M., Friedrich, S., Hall, J. A., Harris, J., Warburton, W. & Cantor, R. (2013). *Appl. Supercond.* **23**, 2400504.

Chen, L. X., Jäger, W. J., Jennings, G., Gosztola, D. J., Munkholm, A. & Hessler, J. P. (2001). *Science*, **292**, 262–264.

Darwin, C. (1914). *Philos. Mag. Ser. 6*, **27**, 675–690.

Doriese, W. B., Adams, J. S., Hilton, G. C., Irwin, K. D., Kilbourne, C. A., Schima, F. J. & Ullom, J. N. (2009). In *The Thirteenth International Workshop on Low Temperature Detectors (LTD13)*, Vol. 1185, pp. 450–453. IEEE.

ESRF (2014). *ID20*, http://www.esrf.eu/home/UsersAndScience/Experiments/Beamlines/content/content/ID20.html, accessed: 08/10/14.

Fano, U. (1947). *Phys. Rev.* **72**, 26–29.

Fischer, D. (2014). *U7A*, http://beamlines.ps.bnl.gov/beamline.aspx?blid=U7A/, accessed: 08/10/14.

Fraser, G., Abbey, A., Holland, A., McCarthy, K., Owens, A. & Wells, A. (1994). *Nucl. Instrum. Methods Phys. Res. A*, **350**, 368–378.

Fuchs, O., Weinhardt, L., Blum, M., Weigand, M., Umbach, E., Bär, M., Heske, C., Denlinger, J., Chuang, Y.-D., McKinney, W., Hussain, Z., Gullikson, E., Jones, M., Batson, P., Nelles, B. & Follath, R. (2009). *Rev. Sci. Instrum.* **80**, 063103.

Fullagar, W., Harbst, M., Canton, S., Uhlig, J., Walczak, M., Wahlström, C. G. & Sundström, V. (2007). *Rev. Sci. Instrum.* **78**, 115105.

Fullagar, W., Uhlig, J., Walczak, M., Canton, S. & Sundström, V. (2008). *Rev. Sci. Instrum.* **79**, 103302.

Gallo, E. & Glatzel, P. (2014). *Adv. Mater.* **26**, 7730–7746.

Glatzel, P., Weng, T.-C., Kvashnina, K., Swarbrick, J., Sikora, M., Gallo, E., Smolentsev, N. & Mori, R. A. (2012). *J. Electron Spectrosc. Relat. Phenom.* **188**, 17–25.

Groot, F. M. F. de & Kotani, A. (2008). *Core Level Spectroscopy of Solids*, *Advances in Condensed Matter Science.* CRC Press.

Haldrup, K., Vankó, G., Gawelda, W., Galler, A., Doumy, G., March, A. M., Kanter, E. P., Bordage, A., Dohn, A., van Driel, T. B., Kjaer, K. S., Lemke, H. T., Canton, S. E., Uhlig, J., Sundström, V., Young, L., Southworth, S. H., Nielsen, M. M. & Bressler, C. (2012). *J. Phys. Chem. A*, **116**, 9878–9887.

Hayashi, H., Kawata, M., Takeda, R., Udagawa, Y., Watanabe, Y., Takano, T., Nanao, S. & Kawamura, N. (2004). *J. Electron Spectrosc. Relat. Phenom.* **136**, 191–197.

Herder, J. W. den *et al.* (2012). *Proc. SPIE*, **8443**, 84432B.

Holland, W. S. *et al.* (2013). *Mon. Not. R. Astron. Soc.* **430**, 2513–2533.

Hudson, A. C., Stolte, W. C., Lindle, D. W. & Guillemin, R. (2007). *Rev. Sci. Instrum.* **78**, 053101.

Huotari, S., Vankó, Gy., Albergamo, F., Ponchut, C., Graafsma, H., Henriquet, C., Verbeni, R. & Monaco, G. (2005). *J. Synchrotron Rad.* **12**, 467–472.

Irwin, K. & Hilton, G. (2005). *Cryogenic Particle Detection*, edited by C. Enss, Vol. 99 of *Topics in Applied Physics*, pp. 63–150. Berlin/Heidelberg: Springer.

Janesick, J. (2001). *Scientific Charge-Coupled Devices.* Bellingham: SPIE Press.

Ketek (2014). *VITUS H7 SDD*, http://www.ketek.net/products/vitus-sdd/vitus-h7/, accessed: 08/10/14.

Kishimoto, S. (1997). *Nucl. Instrum. Methods Phys. Res. A*, **397**, 343–353.

Kleymenov, E., van Bokhoven, J. A., David, C., Glatzel, P., Janousch, M., Alonso-Mori, R., Studer, M., Willimann, M., Bergamaschi, A., Henrich, B. & Nachtegaal, M. (2011). *Rev. Sci. Instrum.* **82**, 065107.

Knoll, G. (2010). *Radiation Detection and Measurement.* Hoboken: John Wiley.

Krings, T., Protić, D., Ross, C., Bombelli, L., Alberti, R. & Frizzi, T. (2014). *J. Instrum.* **9**, C05050.

Lechner, P., Eckbauer, S., Hartmann, R., Krisch, S., Hauff, D., Richter, R., Soltau, H., Strüder, L., Fiorini, C., Gatti, E., Longoni, A. & Sampietro, M. (1996). *Nucl. Instrum. Methods Phys. Res. A*, **377**, 346–351.

Lee, S., Bandler, S., Busch, S., Adams, J., Chervenak, J., Eckart, M., Ewin, A., Finkbeiner, F., Kelley, R., Kilbourne, C., Porst, J.-P., Porter, F., Sadleir, J., Smith, S. & Wassel, E. (2014). *J. Low Temp. Phys.* **176**, 1–7.

Lordi, V., Gambin, V., Friedrich, S., Funk, T., Takizawa, T., Uno, K. & Harris, J. S. (2003). *Phys. Rev. Lett.* **90**, 145505.

Miaja Avila, L., O'Neil, G. C., Uhlig, J., Cromer, C. L., Dowell, M. L., Jimenez, R., Hoover, A. S., Silverman, K. L. & Ullom, J. N. (2015). *Struct. Dynam.* **2**, 024301.

Miaja Avila, L., Silverman, K., Bennett, D., Cromer, C., Dowell, M., Fowler, J., Doriese, W., O'Neil, G., Swetz, D., Uhlig, J., Ullom, J., Yoon, Z., Jimenez, R., Marvel, R. E., Haglund, R. F. & Sundstrom, V. (2013). *CLEO: 2013*, p. QTh4D. 7. Washington: OSA.

Moseley, S. H., Mather, J. C. & McCammon, D. (1984). *J. Appl. Phys.* **56**, 1257–1262.

Neri, L., Tudisco, S., Musumeci, F., Scordino, A., Fallica, G., Mazzillo, M. & Zimbone, M. (2010). *Rev. Sci. Instrum.* **81**, 18–21.

Newbury, D., Irwin, K., Hilton, G., Wollman, D., Small, J. & Martinis, J. (2005). *Cryogenic Particle Detection*, edited by C. Enss, Vol. 99 of *Topics in Applied Physics*, pp. 267–312. Berlin/Heidelberg: Springer.

Noroozian, O., Mates, J. A. B., Bennett, D. A., Brevik, J. A., Fowler, J. W., Gao, J., Hilton, G. C., Horansky, R. D., Irwin, K. D., Kang, Z., Schmidt, D. R., Vale, L. R. & Ullom, J. N. (2013). *Appl. Phys. Lett.* **103**, 202602.

Oxford (2014). *SDD-X-MaxN*, http://www.oxford-instruments.com/products/microanalysis/energy-dispersive-x-ray-systems-eds-edx/eds-for-sem/sdd, accessed: 08/10/14.

Roosbroeck, W. van (1965). *Phys. Rev.* **139**, A1702–A1716.

Sa, J. (2014). *High-Resolution XAS/XES*. Boca Raton: CRC Press.

Schoonjans, T., Brunetti, A., Golosio, B., Sanchez del Rio, M., Solé, V. A., Ferrero, C. & Vincze, L. (2011). *Spectrochim. Acta B*, **66**, 776–784.

Schülke, W. (2007). *Electron Dynamics by Inelastic X-ray Scattering.* Oxford University Press.

Shiki, S., Ukibe, M., Kitajima, Y. & Ohkubo, M. (2012). *J. Low Temp. Phys.* **167**, 748–753.

Smith, S., Adams, J., Bailey, C., Bandler, S., Chervenak, J., Eckart, M., Finkbeiner, F., Kelley, R., Kilbourne, C., Porter, F. & Sadleir, J. (2012). *J. Low Temp. Phys.* **167**, 168–175.

Sobott, B. A., Broennimann, Ch., Schmitt, B., Trueb, P., Schneebeli, M., Lee, V., Peake, D. J., Elbracht-Leong, S., Schubert, A., Kirby, N., Boland, M. J., Chantler, C. T., Barnea, Z. & Rassool, R. P. (2013). *J. Synchrotron Rad.* **20**, 347–354.

Stiehl, G. M., Doriese, W. B., Fowler, J. W., Hilton, G. C., Irwin, K. D., Reintsema, C. D., Schmidt, D. R., Swetz, D. S., Ullom, J. N. & Vale, L. R. (2012). *Appl. Phys. Lett.* **100**, 072601.

Szymkowiak, A., Kelley, R., Moseley, S. & Stahle, C. (1993). *J. Low Temp. Phys.* **93**, 281–285.

Tan, H., Breus, D., Hennig, W., Sabourov, K., Warburton, W. K., Doriese, W., Ullom, J. N., Bacrania, M. K., Hoover, A. S. & Rabin,

electronic reprint

M. W. (2008). *Proceedings of the 2008 Nuclear Science Symposium Conference Record (NSS'08)*, pp. 1130–1133. IEEE.

Uhlig, J. (2011). *Life of a Photon in X-ray Spectroscopy*, PhD thesis, Lund University, Sweden. (http://www.jensuhlig.de/Thesis_Jens.pdf, accessed: 08/10/14.)

Uhlig, J., Fullagar, W., Ullom, J. N., Doriese, W. B., Fowler, J. W., Swetz, D. S., Gador, N., Canton, S. E., Kinnunen, K., Maasilta, I. J., Reintsema, C. D., Bennett, D. A., Vale, L. R., Hilton, G. C., Irwin, K. D., Schmidt, D. R. & Sundström, V. (2013). *Phys. Rev. Lett.* **110**, 138302.

Uhlig, J., Wahlström, C.-G., Walczak, M., Sundström, V. & Fullagar, W. (2011). *Laser Particle Beams*, **29**, 415–424.

Ullom, J. N., Beall, J. A., Doriese, W. B., Duncan, W. D., Ferreira, L., Hilton, G. C., Irwin, K. D., Reintsema, C. D. & Vale, L. R. (2005). *Appl. Phys. Lett.* **87**, 194103.

Vankó, G., Bordage, A., Glatzel, P., Gallo, E., Rovezzi, M., Gawelda, W., Galler, A., Bressler, C., Doumy, G., March, A. M., Kanter, E. P., Young, L., Southworth, S. H., Canton, S. E., Uhlig, J., Smolentsev, G., Sundström, V., Haldrup, K., van Driel, T. B., Nielsen, M. M., Kjaer, K. S. & Lemke, H. T. (2013). *J. Electron Spectrosc. Relat. Phenom.* **188**, 166–171.

Vankó, G., Neisius, T., Molnár, G., Renz, F., Karpáti, S., Shukla, A. & de Groot, F. M. F. (2006). *J. Phys. Chem. B*, **110**, 11647–11653.

Verhoeve, P., Martin, D., Venn, R., Verhoeve, P., Martin, D. D. E. & Venn, R. (2010). *Proc. SPIE*, **7742**, 74420O1.

Vila, F. D., Jach, T., Elam, W. T., Rehr, J. J. & Denlinger, J. D. (2011). *J. Phys. Chem. A*, **115**, 3243–3250.

Wollman, D. A., Nam, S. W., Hilton, G. C., Irwin, K. D., Bergren, N. F., Rudman, D. A., Martinis, J. M. & Newbury, D. E. (2000). *J. Microsc.* **199**, 37–44.

electronic reprint